TITLE

Radiant heating floors with PCM bands for thermal energy storage: A numerical analysis.

AUTHOR NAMES AND AFFILIATIONS

B. González and M.M. Prieto*

University of Oviedo, Energy Department, Campus de Viesques, 33204 Gijón, Asturias, Spain

(*) Author for correspondence: email: manuelap@uniovi.es

ABSTRACT

Radiant heating floors with phase change materials (PCMs) for thermal energy storage (TES) represent an opportunity to achieve improvements in energy efficiency in buildings. In radiant floors that include PCM in macro-capsules the thermal energy is stored during melting and subsequently released during solidification. This paper presents a CFD study for hydronic radiant heating floors with PCM bands embedded in a concrete core in accordance with several arrangements depending on the band width and position with respect to the heating pipes. The heat transfer solutions are compared with those obtained for radiant floors without PCM. Other effects analysed are: the thickness of a wooden cover, which represents the main thermal resistance of the floors, the indoor air temperature and the heating pipe surface temperature. The results show that PCM radiant floors increase thermal energy storage up to 243% and decrease the maximum heat flux between 10 and 18% according to the case. They also release the heat slowly when the heating is off. The time-averaged heat fluxes during the solidification process are between 31.4 and 44.6 W/m^{2}and the solidification last for more than 24 hours, allowing time to start a new charge using for instance solar energy.

KEYWORDS

Charge-discharge; RT28HC paraffin; phase change materials: radiant heating floors; thermal energy storage

NOMENCLATURE

A	Area of the cell surfaces (m^2)
A_{mush}	Constant in Eq. (6) (kg/s m^3)
a	Distance between PCM bands and the centre of the pipe (m)
b	PCM band width (m)
c_p	Specific heat at constant pressure (J/kgK)
D	Outer pipe diameter (mm)
E	Energy per unit of floor surface (Wh/m^2)
f	Fin coefficient (m^{-1})
$\vec{g}$	Acceleration due to gravity (m/s^2)
h	Heat transfer coefficient (W/m^2K)
i	Specific enthalpy (J/kg)
j	Index indicating cells in Eq. (7-9)
k	Thermal conductivity (W/mK)
M	Spacing between the centres of the pipes (m)
p	Pressure
$\dot{q}$	Heat flux (W/m^2)
$\bar{\dot{q}}$	Heat flux averaged over time (W/m^2)
R	Thermal resistance (m^2K/W)
S_m	Volumetric momentum source term (N/m^3) in Eq. (6)
T	Temperature (°C)
th	Thickness (m)
U	Overall heat transfer coefficient (W/m^2K)
V	Volume of the cell (m^3)
$\vec{v}$	Velocity vector (m/s)
$\vec{v}_p$	Drag velocity vector of the solid phase (m/s)
x	Length coordinate of the floor surface (m)

Greek symbols

β	Volumetric liquid fraction of the PCM (-)
Δt	Time-step (s)
ΔT_{melt}	Melting range (ºC)
ε	Constant in Eq. (6) (-)
η	Efficiency (-)
λ	Phase change enthalpy of the PCM (kJ/kg)
μ	Dynamic viscosity (kg/ms)
ρ	Density (kg/m^3)
$\bar{\bar{\tau}}$	Shear stress tensor (N/m^2)

Subscripts

avg	Averaged
bhp	Below heating pipes
bs	Bottom surface
c	Cover
char	Charge
conc	Concrete
dis	Discharge
fs	Floor surface
hp	Heating pipes
iair	Indoor air
ins	Insulation
liq	Liquid
pcm	Phase change material
soli	Solid temperature of the PCM
ss	Steady state

tot	Total
uhp	Upper heating pipes

Acronyms

CFD	Computational Fluid Dynamics
DFST	Difference Floor Surface Temperature
FDM	Finite Difference Method
FEM	Finite Element Method
FVM	Finite Volume Method
MFST	Maximum Floor Surface Temperature
PCM	Phase Change Material
STC	Spanish Technical Code
TES	Thermal Energy Storage
TSI	Denomination for the method in [37] proposed by ASHRAE

1. INTRODUCTION

Radiant heating floors are widely used in buildings as they provide advantages such as efficient use of space and uniform distribution of temperature, which produces improved thermal comfort. Furthermore, they can operate at low water temperatures with the consequent increase in the efficiency of the thermal generators [1] and a high level of self-regulation [2]. Appropriate system design is essential to maintain comfort conditions with adequate heat flux at the surface of the floor and suitable surface temperature distribution [3]. There are standards, scientific documents and technical guides that provide design criteria for sizing radiant heating floors [4, 5], while numerous studies have established the theory of radiant systems demonstrating their viability to control indoor conditions in the building efficiently [6]. Thermal energy storage (TES) with phase change materials (PCM) allows not only compact storage, but also isothermal release of heat or cold [7] and is increasingly used in many thermal systems to achieve a more efficient use of energy [8, 9]. Furthermore, PCMs may be included in building elements, providing greater thermal storage within a narrow temperature range [10-13].

As for the type of research carried out, there are mathematical and experimental approaches and there is also a wide variety of applications with combinations of types of radiant floors and thermal systems. Lin et al. [14, 15] numerically [15] and experimentally [14] investigated an under-floor electric heating system with shape-stabilized PCM plates. A full model [15] was developed using the FDM for a test room with under-floor heating powered with electric heaters that included a PCM layer over them. The heat transfer was considered one-dimensional and conduction-based. Results showed good performance: the energy was stored overnight in the PCM using cheap electricity and discharged during the day. Barzin et al. [16] experimentally studied an under-floor heating system based on a gypsum board impregnated with PCM for space heating developing a price-based control system which achieved electricity savings in terms of consumption and cost of up to 35% and 44.4%, respectively. Cheng et al. [17] theoretically and experimentally studied the effect of the thermal conductivity of the PCM in an under-floor heating system with a shape-stabilized PCM layer charged with cheap, nighttime electricity.

Jin and Zhang [18] proposed a double PCM layer, one for heating and the other for cooling, for an hydronic radiant floor with one row of pipes embedded in a concrete core below PCM layers. These authors studied the thermal performance of a test room following an FDM conduction-based numerical approach coupled with a one-dimensional radiant heating floor. Numerical results showed that the energy released by the radiant floor in peak periods increased between 41.1% and 37.9% compared to conventional systems. Xia et al. [19] experimentally studied a hydronic radiant floor system with a double layer of PCM with two rows of heating and cooling pipes embedded in two different PCMs that can work both in summer and winter.

Cabrol and Rowley [20] simulated a building with an air-source heat pump system coupled to a simplified floor slab-embedded PCM for the purposes of the TRNSYS simulation. They concluded that the PCM floor slab improves the temperature stability during the heating season and reduces the risk of overheating during the summer for a high-performance building. Mazo et al. [21] developed a test room model to simulate a hydronic radiant floor system with the PCM embedded in it. The system was powered by means of a heat pump and the savings in electricity consumption costs were close to 18% compared to a conventional case. Lu et al. [22] designed a new radiant floor in which the circumference of the outer pipe was wrapped with a layer of PCM and mathematically modeled following a one-dimensional FVM approach. This hydronic radiant floor was simulated in TRNSYS coupled to a solar water heating system and was validated for full-scale experiments.

Huang et al. [23] numerically and experimentally studied a new type of hydronic radiant heating floor with capillary pipes placed above and below a concrete skeleton in which the empty cavities were stuffed with macro-encapsulated PCM.A two-dimensional FEM conduction-based approach was developed and implemented using ANSYS. The results showed that the PCM can release 3419 kJ/m^2 for 16 h in the discharge period, which represented half of the energy supplied during the charge.

Zhou and He [24] carried out experiments to investigate the performance of a low-temperature hydronic radiant floor with two types of heating pipes (conventional poly-ethylene coils and capillary mat) embedded in a sensible or latent thermal mass for heat storage, using sand and PCM, respectively. In addition, these authors applied a two-dimensional conduction-based model which they successfully compared with experimental data. The results showed that radiant floors with a capillary mat provide a more uniform temperature profile and that a shorter time was needed to reach the same room temperature. Regarding the heat release, results show that it lasts double of time using PCM than using sand as thermal mass.

Zhao et al. [25] established a two-dimensional FLUENT-based CFD model employing an enthalpy-porosity approach [26, 27] to model convection-diffusion mushy region phase-change for a hydronic PCM radiant floor coupled with an air cavity in which the pipes were fully covered by the PCM layer. They analysed the PCM liquid fraction and temperature contours, finding that the PCM thermal conductivity played a major role in maintaining the air temperature of the room during solidification. Moreover, these authors proposed a new floor heat storage structure based on a combination of concrete and PCM in the slab to accelerate the increase in air temperature.

The literature review shows that several kinds of radiant floors including PCM have been studied following different approaches and geometrical configurations. PCM embedded in radiant heating floors allows storing energy during the phase change, thus enhancing the use of cheap power [14-17, 21] or renewable energy [22-24]. However, there is still a shortage in the literature about the comparison of classical methods of calculating radiant floors and multidimensional methods. In addition, there is still a shortage of research on the study of effects related to the use of PCM, as those concerning its placement, relationship with other materials included in the hydronic radiant floor (heating pipes, concrete or mortar and cover) and operating conditions that affect the overall performance of the system.

This paper discusses the heat transfer performance of hydronic radiant floors that include phase change materials using a 2D approach. In the proposed PCM radiant floors, the PCM is incorporated in alternating bars, macro-capsules, embedded in a concrete core. Two basic arrangements will be studied: a) long parallelepiped PCM bars containing one pipe inside, and b) two narrower parallelepiped PCM bars arranged symmetrically between the heating pipes without direct contact with these pipes. These designs have some differences with respect to alternative designs from literature as the skeleton of concrete cavities filled with PCM proposed by Huang et al. in [23] and the system of pipes completely embedded PCM suggested by Lu et al. in [25]. Both arrangements have been designed with a concrete core structure that takes into account the relative position between the PCM and the heating pipes: PCM_A (one heating pipe embedded in PCM and the other not) and PCM_B (both heating pipes integrated in concrete core). An asymmetric distribution of the PCM is tested in the PCM_A design to discover how heat diffuses and to find out the temperature differences observed at the level of the underfloor heating surface. On the other hand, the asymmetric arrangement with alternatively integrated tubes also simplifies the construction of underfloor heating.

The CFD enthalpy-porosity approach is used for the phase change calculations to model the convective effects in the PCM subdomains. Next to this, in order to compare the thermal performance with classical radiant floors, which do not contain PCM inside, two classical radiant floors based on concrete or high thermal conductivity mortar will be analysed. For the classical radiant floors, the heat fluxes will be compared using CFD conduction-based models and ASHRAE procedures in order to increase the number of cases comparing calculation methods.

The study will consider both the charge and discharge periods. The charge period is understood as the time during which water circulates through the heating pipes (the temperature of the floor starts with a constant value which is the same of the heated room) and the floor is heated while the mass of PCM is melted. The period of discharge corresponds to the time when the circulation of water inside the pipes is interrupted and the floor releases heat until the entire PCM solidifies.

2. MODELLING

2.1. Physical model

A schematic view of the two-dimensional computational domains (classical and PCM radiant floors) is shown in Fig. 1: a) conventional radiant floor with concrete as thermal mass and the heating pipes placed near the top of the concrete; b) Conventional floor with improved thermal conductivity mortar and heating pipes placed near the insulation; c) PCM underfloor heating with concrete core and long PCM bands with the heating pipes embedded alternately in the PCM or in concrete, PCM_A, and d) PCM radiant floor with a concrete core and two narrower PCM bands arranged symmetrically between the heating pipes without direct contact between the PCM and the pipes, PCM_B.

The geometric dimensions are the following: wooden cover thickness, th_c, taking values of 10 and 20 mm; thickness of the insulation, th_{ins}=50 mm; outer heating pipe diameter, D=20 mm; spacing between the centres of the pipes, M=200 mm. Two thicknesses of concrete or mortar above and below the pipes will be considered for classical radiant floors, depending on whether concrete or mortar is used. Above the pipes, th_{uhp}=10 mm and th_{uhp}=40 mm, which correspond to the thicknesses below pipes th_{bhp}=30 mm and 0 mm, respectively. For the PCM radiant floors, the thicknesses of concrete above or below the pipes will be th_{uhp}=10 mm and th_{bhp}=30 mm. For PCM_B the dimensions a= 20 mm and b=47.5 mm of the PCM bands were obtained by keeping the same volume of PCM in both PCM floors.

The melting temperature of the PCM should be below the usual temperature for water in the hydronic floor, approximately 40ºC, and slightly higher than the recommended temperature for the floor surface, 25-26 ºC. The PCM used in the study is RT28HC paraffin [28, 29], with properties in [30] and that has a latent heat of 224 kJ/kg and a melting temperature range between 27 and 29ºC corresponding to T_{soli} and T_{liq} respectively, similar temperatures are tested in [21, 31] . The properties of the PCM, concrete, conductive mortar, wooden cover and XPS insulation subdomains are shown in Table 1.

The boundary conditions are of symmetry at the right and left sides of the floor domain. For the heating pipe: fixed temperature or zero heat flux at the outer surface of the pipe, depending on the process, charge or discharge, respectively. The condition of fixed temperature during the charge (melting of the PCM) is adequate because the high convective heat transfer coefficient of the water relatively to the low conductivity and the high thermal inertia of the material surrounding the pipe. The condition of zero heat flux is due to the fact that, during the discharge (solidification of the PCM), the heating water pumps are turned off and the heat accumulated in the water can be neglected relative to the heat accumulated in the floor materials and it dissipates quickly. For the heat transfer coefficient at the floor surface, h_{fs}=10 W/m^{2}K will be considered for simultaneous natural convection and radiation in accordance with the Spanish Technical Code STC [32]. At the lower surface of the insulation material, the conductance considered is U_{bs}=2 W/m^{2}K, which was calculated as the inverse of the total thermal resistance: sum of one due to a 300 mm concrete base, which supports the floor, and another that combines the resistances in parallel due to natural convection and radiation from the room below, all in accordance with the STC.

In order to study the floors under different heating conditions, a parametric study was performed. They were considered two values for wooden cover thickness: 10 and 20 mm; three temperatures during the charge for the surface of the heating pipesT_{hp}: 35, 40 and 45ºC; and another three temperatures for the indoor air temperature T_{iair}: 18, 20 and 22ºC, the last values near the comfort temperature of 20ºC. With respect to the surface temperature of the heating pipes, these values were chosen to guarantee a good activation of the melting process during the charge period and, with respect to the air temperature, to cover small temperature oscillations of the surrounding indoor air, being the typical heating set point temperature 20 ° C.

The conservation equations were solved using the commercial CFD software ANSYS Fluent. The following energy equation, Eq. (1), was used for the solid subdomains such as the wood cover, concrete, mortar and insulation.

$$\frac{\partial}{\partial t}(\rho i) = \nabla \cdot (\mathrm{k}\nabla \mathrm{T}) \tag{1}$$

In solidification only conduction influences, but in fusion natural convection become important. To obtain heat transfer rate in PCM considering natural convection, most studies apply the enthalpy-porosity method to predict temperature distributions more accurately as in [33-38] and this method is the reference one for phase change in ANSYS Fluent. On the other hand, most of the models for PCM studies in the literature only consider conduction heat transfer. This enthalpy-porosity model has been validated in the literature as in [39-41].

The enthalpy-porosity formulation developed by Voller et al. [26, 27] was used for the PCM subdomains. In this approach, the liquid-solid mushy zone that represents the phase change region is treated as a porous zone whose porosity is equal to the volumetric liquid fraction. The volumetric liquid fraction, β, is defined as the fraction of the cell volume that is in liquid form. Porosity ranges between 0 and 1, depending on the status of the phase change process.

The conservation equations for mass and energy in the PCM subdomain are given in Eqs. (2, 3):

$$\frac{\partial\rho}{\partial t} + \nabla\cdot(\rho\vec{v}) = 0 \tag{2}$$

$$\frac{\partial}{\partial t}(\rho i) + \nabla\cdot(\rho\vec{v}i) = \nabla\cdot(k\nabla T) \tag{3}$$

The solution of the problem is obtained following CFD methodology in ANSYS Fluent solving the continuity and energy equations, Eqs. (2, 3), and the liquid fraction equation, which follows Eq. (4), defined in terms of the temperature of the cell and range of phase change temperatures ($T_{soli} \le T \le T_{liq}$).

$$\begin{aligned} &\beta = 0 && \text{if} \quad T < T_{soli} \\ &\beta = 1 && \text{if} \quad T > T_{liq} \\ &\beta = \frac{T - T_{soli}}{T_{liq} - T_{soli}} && \text{if} \quad T_{soli} \le T \le T_{liq} \end{aligned} \tag{4}$$

As regards the momentum equation, Eq. (5), the source term expressed by Eq. (6), $\vec{S}_m$, is added due to the reduced porosity in the mushy zone:

$$\frac{\partial}{\partial t}(\rho\vec{v}) + \nabla\cdot(\rho\vec{v}\vec{v}) = -\nabla \mathrm{p} + \nabla\cdot(\bar{\bar{\tau}}) + \rho\vec{g} + \vec{S}_m \tag{5}$$

$$\vec{S}_m = \frac{(1-\beta)^2}{(\beta+\varepsilon)} A_{mush}\left(\vec{v} - \vec{v}_p\right) \tag{6}$$

The term ε is a small number (0.001) to avoid division by zero, A_{mush} is the mushy zone constant, which measures the amplitude of the damping (the higher this value, the steeper the transition of the material velocity to zero as it solidifies), and $\vec{v}_p$ accounts for the movement of the solidified material outside the domain, which is equal to 0 for this case.

The results calculated following Eqs. (7-9) in the cells at each time-step, were: the volume-averaged liquid fraction in the PCM subdomains, the area-weighted average temperatures and heat fluxes at the floor, bottom and heating pipe surfaces.

$$\beta_{avg} = \frac{1}{V}\int_V \beta\, dV = \frac{1}{V}\sum_{j=1}^{n} \beta_j |V_j| \tag{7}$$

$$\left(T_{fs}, T_{bs}\right) = \frac{1}{A}\int_A T dA = \frac{1}{A}\sum_{j=1}^{n} T_j |A_j| \tag{8}$$

$$\left(\dot{q}_{fs}, \dot{q}_{bs}, \dot{q}_{hp}\right) = \frac{1}{A}\int_A \dot{q} dA = \frac{1}{A}\sum_{j=1}^{n} \dot{q}_j |A_j| \tag{9}$$

2.3. Numerical procedure

The conservation equations were solved considering second-order implicit transient formulation. A second-order upwind scheme was used for the spatial discretization and the SIMPLE algorithm with PRESTO scheme for the pressure-velocity coupling. It was found that the solution is convergent and the minimum residue level (10^{-10} - 10^{-15}).

In order to define the grid size, the case of th_c= 20 mm, T_{iair}= 20ºC, T_{hp}= 40ºC was chosen. Floor domains were initialized at 20ºC. Grid tests for solution independence were performed for the PCM radiant floors using three grids, varying the refinement level. Because of floors with PCM are more dependent on the refinement level, the grid parameters obtained for the PCM floors test were also used for the conventional floors. Table 2 shows the number of elements and the average and standard deviation of the mesh quality, values closer to 1 indicating higher quality mesh [42]. All the grids present high average quality with little deviation. Fig. 2 presents the results of the grids test for a time-step, Δt=0.5 s, which value was choosen after testing several alternatives. The solution becomes independent of the grid from grid refinement nº 2 onwards in both PCM radiant floors; hence this grid was selected.

Natural convection can be the dominant mechanism of heat transfer in the melting processes and its influence varies greatly with the dimensionless Rayleigh and Stefan numbers, the aspect ratio of the PCM container, the location of the heating pipes and the boundary conditions imposed [43]. As regards the realiability of the entalpy-pososity model, several studies have successfully compared this model with experimental data [25, 39-41, 44]. For the enthalpy-porosity model, the parameter that controls the melting rate in the solid-liquid transition is A_{mush}. The recommended value according to the ANSYS Fluent theory guide [45] is 10^5. This value was also used in previous papers [37-38, 44-] and was therefore chosen for both geometries.

2.4. Steady-state heat transfer rate calculation

The heat transfer rate for classical radiant floors under steady-state conditions may be calculated using Eqs.(10-13) following the method in [46], which is proposed by ASHRAE [4]. This procedure is being used for design purposes and was successfully compared with experimental data in [3]. The TSI model is for permanent regime and is the one that is most recognized and complete that appears in the ASRHAE standards. However, has the limitation of not to take into account heterogeneities in the installation of the different materials and not consider non-linear thermal diffusivity. Even taking into account these limitations when our proposed model reaches the steady state, the TSI methodology can be adapted with better success in solidification, which is the most interesting process because it is the slowest phase change process and when the heat is dissipated into the room. In TSI method, the calculation of the steady-state heat flux, $\dot{q}_{fs,ss}$, considers the transverse heat diffusion using an equivalent fin coefficient, f, expressed in Eq. (12). The heat flux depends on the operating conditions and thermal resistances above the heating pipes, $R_{uhp} = th_{uhp}/k_{uhp}$ and $R_c = th_c/k_c$, as well as on the fin efficiency, η.

$$T_{hp} \approx T_{iair} + \frac{\dot{q}_{fs,ss} M}{h_{fs}[M + D(1-\eta)]} + \dot{q}_{fs,ss}(R_{uhp} + R_c) \quad (10)$$

$$\eta = \frac{2}{f(M-D)} \tanh\left[f \frac{(M-D)}{2}\right] \quad (11)$$

$$f = \left[\frac{h_{fs}}{\left(2 + \frac{R_c}{R_{uhp}}\right)\left(k_{uhp} th_{uhp} + k_c th_c\right)}\right]^{\frac{1}{2}} \quad (12)$$

$$R_{tot} = R_{uhp} + R_c + \frac{1}{h_{fs}} \quad (13)$$

Concerning the resistances above the heating pipes, k_c is the conductivity of the cover and k_{uhp} the conductivity of concrete or mortar.

Concerning the PCM radiant floors, an equivalent thermal conductivity approach is proposed for the layer of thickness th_{uhp}. This conductivity will be based on a parallel resistance calculation: concrete and PCM macro-capsules. For both PCM radiant floors, it was defined as the mean conductivity of the concrete and the PCM macro-capsule, Eq. (14).

$$k_{uhp} = \left(k_{pcm} + k_{conc}\right)/2 \quad (14)$$

2.5. Application to steady and transitory regimens

Steady-state and transient heat transfer in the radiant floors are analysed. For the radiant floor including PCMs, during charging, the temperature at the surface of the heating pipes T_{hp} is maintained and the provided energy is stored in the floor's thermal mass (sensible or latent thermal energy) and is transmitted to the room. For the present study, the duration of the charge will be kept at six hours for all the analysed cases, after which the discharge will begin. During the discharge, the heat flux at the surface of the heating pipes, $\dot{q}_{hp}$ will be considered zero and the thermal energy stored by the floor's thermal mass during the charge will be released to the room. The end of the discharge time will be considered as the point at which the PCM becomes completely solidified.

First, the heat transfer rates for the steady-state are obtained depending on T_{hp} and th_c with T_{iair}= 20ºC. Subsequently, the transient heat transfer during the charge and the discharge are analysed. They are studied the contours of the melted liquid fraction in the PCM subdomains and of the temperature in the complete domains, and besides, the floor surface temperature distribution for the case: th_c=20 mm, T_{hp}=40ºC and T_{iair}=20ºC. The volume-averaged liquid fraction in the PCM subdomains and the heat fluxes during the charge and discharge processes for the two cover thicknesses are studied as well, along with the thermal energy balances, which allow compare the radiant floors that include PCMs and the classical radiant floors for fixed operating conditions of T_{hp}=40ºC and T_{iair}=20ºC and for the two cover thicknesses th_c. Finally, a parametric study for the PCM floors was performed in terms of th_c, varying the values of T_{hp} and T_{iair}. Melting and solidification times and time-averaged heat fluxes at the floor surface during the charge and discharge processes are likewise discussed.

3. RESULTS AND DISCUSSION

3.1. Main parameters and steady-state heat transfer rates

In accordance with the previously explained calculations, Table 3 shows the main parameters of the analysed PCM floors, according to Eqs. (10-14).

Fig. 3 presents the steady-state heat flux, which is the maximum heat transfer rate transmitted at the radiant floor surface, for T_{iair}=20ºC and depending on T_{hp} and th_c. These heat fluxes are obtained using the CFD model and the method proposed by ASHRAE, with acronym TSI, Eqs. (10-14). This is The maximum heat flux range, 50-110 W/m^2 for the classical radiant floor with the pipes embedded in the concrete, 60-130 W/m^2 for the classical radiant floor with the pipes embedded in the mortar, and 45-90 W/m^2 for the PCM radiant floors. This decrease in maximum heat transfer rates for the PCM radiant floors is due to the low conductivity of the PCM compared to classical materials (all concrete or mortar), which produces an increase in the total thermal resistance, R_{tot} and a decrease in efficiency, η. Generally, the results show a good fit between both calculation procedures with linear behaviour, similar slope, and small offsets. However, it is important to note that with the lowest cover thickness (10mm) and the lowest heating pipe surface temperature (Thp = 35 ° C), the CFD procedure differs by up to 15%, showing a nonlinear trend in both configurations (PCM_A and PCM_B). These results indicate that the steady state heat flux calculation for PCM floors using the TSI procedure should be performed with a sufficient temperature gradient between the heating pipe and the PCM melting point to decrease the effect of nonlinearities, especially when PCM is poorly insulated. Another difference to consider between two procedures is that TSI assumes one-dimensional heat transfer while CFD is based on a two-dimensional model.

3.2. Melted liquid fraction, temperature contours and floor surface temperature distribution

The liquid fraction in the PCM subdomains for both PCM radiant floors at different charge times are given in Fig. 4, The liquid fraction contours are plotted for three volume-averaged liquid fraction values (β_{avg}): 0.3, 0.6 and 0.95. The maximum, β_{max}, and minimum, β_{min}, values are also calculated. The aspect of the contours differs substantially. For the case of PCM_A, the solid-liquid interphase progresses from the heating pipe sideward and downwards with large melting zones: liquid ($\beta = 1$) in red and solid ($\beta = 0$) in blue. For the case of PCM_B, the melting progresses from the hot sides upwards, the contours in both PCM macro-capsules are symmetrical and the solid-liquid interphase is less defined with a smoother transition.

The temperature contours are plotted in Fig. 5 at different charge and discharge times for all the analysed radiant floors. The floor temperature field is symmetric for all the floors except little differences caused by the PCM distribution in floor PCM_A. During the charge, the classical floors heat faster than the PCM floors. The area-weighted average temperatures at the floor surface, T_{fs}, at the end of the charge are respectively 26.5ºC and 27.3ºC for the concrete and mortar floors, and 25.6ºC and 25.3ºC for the PCM_A and PCM_B floors. During the discharge, the classical radiant floors change temperature faster than the PCM radiant floors, showing the very good accumulative effect of the PCM, as the floor remains warm for a much longer time. In the last time analysed, 21 h, the area-weighted average temperatures at the floor surface are respectively 20.9ºC and 20.7ºC for the classical radiant floors (concrete and mortar), and 23.1ºC and 23.4ºC for both PCM radiant floors.

The temperature distribution at points *x* (from 0 to 20 cm) at the floor surfaces are represented against time in Fig. 6. Charge and discharge times are indicated with continuous and discontinuous lines respectively. The melting progress is highly influenced by the relative position of the heating pipes and PCM macro-capsules. Temperature distribution results are summarized in Table 4 according to the maximum floor surface temperature (MFST) and the difference between the maximum and minimum floor surface temperatures (DFST). These parameters are related to thermal comfort standards [3-5]: on the one hand, the MSFT must be limited; on the other, low values of DFST are desired for thermal comfort. The highest MSFT value occurs at the last instant of the charge (after six hours). This value is around 28ºC for all the floors. As to the DFST, significant differences exist between floors. The PCM floors have higher DFST values than the classical floors. During the discharge, the DFST falls rapidly for all floors except for PCM_A, in which the DFST first decreases and then increases because the concrete cooled faster than the PCM. PCM_A is slightly less recommended from the point of view of thermal comfort than PCM_B, because during the discharge the DFST difference has a value of 0.3ºC in PCM_B compared to a DFST value of 1.4ºC for PCM_A. The best performance is obtained with the mortar floor due its higher conductivity, providing the greatest uniformity in temperature distribution during both the charge and discharge processes.

3.3. Volume-averaged liquid fraction, heat fluxes and thermal energy balance

The evolution of the volume-averaged liquid fraction in the PCM floors during the charge and discharge processes and of the heat flux at the surfaces of the heating pipes during charging are presented in Fig. 7 for the four types of radiant floors as a function of the thickness of the cover. Regarding the evolution of the volume-averaged liquid fraction, the melting processes have finished before the end of the charge, which was fixed at six hours. The melting is faster for PCM_A than for PCM_B, while the cover thickness (10 or 20 mm) hardly influences the duration of this process (1.38 and 1.41h for PCM_A and 4.21 and 4.10 h for PCB_B). Nevertheless, the influence of the cover thickness during solidification is notable, the duration of the process being 24.31 and 31.19 h for PCM_A, and 19.56 and 25.65 h for PCM_B, respectively. Thus, decreasing the cover thickness from 20 to 10 mm increases the solidification speed to 24% in floor PCM_A and to 22% in PCM_ B. The heat fluxes then decrease to similar values to those of the other radiant floor arrangements. The average heat fluxes at the surface of the radiant floors during the charge and discharge processes are plotted in Fig. 8. The heat fluxes increase during charging from zero to the maximum after six hours. At the end of the charge, these values approach the heat fluxes for the steady-state. Depending on the type of radiant floor and the cover thickness (10 and 20 mm), the heat fluxes obtained for the classical radiant floors are 83.5 and 65.2 W/m^2 for the concrete radiant floor and 93.6 and 73.2 W/m^2 for the mortar radiant floor. For the PCM radiant floors, these values are 71.0. and 55.6 W/m^2 for PCM_A, and 70.2 and 53.4 W/m^2 for PCM_B. Therefore, the PCM radiant floors take more time to charge and the steady-state maximum heat fluxes are lower.

During the discharge process, the averaged heat fluxes at the surface of the floor decrease from the maximum heat flux, which is reached during charging, to zero when thermal equilibrium is reached. In Fig. 8, the behaviour of the PCM radiant floors was plotted only until the PCM became solidified, at which point there is still sensible thermal energy to release, and hence the time at which it becomes zero has still not been reached. In the classical radiant floors, the heat flux falls rapidly, the heat fluxes being below 20 W/m^2 in all the cases 10 hours after the discharge commences. In the PCM radiant floors, the heat fluxes initially decrease rapidly, but then decrease slowly, due to the stored latent heat, remaining at high levels during long periods (more than twelve hours). The time-averaged heat fluxes during the discharge process for cover thicknesses of 10 and 20 mm are respectively 37.9 and 31.4 W/m^2 for PCM_A and 44.6 and 35 W/m^2 for PCM_B. This behavior is highly suitable if the supplied heat fluxes are enough to maintain conditions of comfort in the rooms where these floors may be installed. The heat fluxes are maintained for more than 24 hours, allowing time to start a new charge obtained, for instance, from solar energy.

Table 5 shows the thermal energy balances per unit of floor surface: supplied, released and stored energies during the charge and complete discharge up to thermal equilibrium (uniform floor temperature equal to indoor air temperature)**.** The thermal energy stored (TES) during the charge is calculated according to Eq.(15), the energy supplied by the heating pipes being found to be 160-180% higher for the PCM floors than for the classical floors. The thermal energy stored ranges between 445.5 and 552.0 Wh/m^2 for the classical radiant floors and between 1141.0 and 1245.5 Wh/m^2 for the PCM radiant floors. The amount of stored energy due to the PCM is 731.5 Wh/m^2. Hence, there is an increase of 243% compared to the classical floors. The TES percentage in the last column is calculated with respect to the energy supplied by the heating pipes; for the classical radiant floors, this percentage ranges between 46.8-63.7%, the highest value being obtained for the concrete floor and a cover thickness 20 mm. Similarly, for PCM radiant floors, this percentages ranges between 74.7-82.8%.

$$TES = E_{hp} - E_{fs,char} - E_{bs,char} \qquad (15)$$

Regarding the ratio of thermal energy transmitted to the heated room during the discharge with respect to the charge period, columns fourth and sixth, the PCM radiant floors have ratios ranging between 2.9 and 4.7 depending on the arrangement and the cover thickness. With a cover thickness of 20 mm, PCM_ B has the highest ratio, whilst PCM_A, with a 10 mm cover thickness, has the lowest ratio of the PCM radiant floors. For classical floors, these ratios range between 0.9 and 1.4 with the same behaviour with respect to th_c, the highest ratios for the classical floors being obtained for the concrete floor. The percentage of losses through the bottom surface does not fall below 10% for any case and fundamentally depends on the cover thickness.

3.4. Performance of PCM radiant floors depending on heating conditions

In this section, the PCM radiant floors are analysed under different heating conditions: temperature at the surface of the heating pipes, T_{hp}, indoor air temperature of the heated room, T_{iair}, and cover thickness. Melting and solidification times and time-averaged heat fluxes transmitted, $\dot{\bar{q}}_{fs}$, to the heated room at the floor surface during charging and discharging are plotted in charts in Figs. 9 and 10, respectively.

The duration of the phase change processes shown in Fig. 9 decreases with T_{hp} and T_{iair} during melting and increases during solidification with extreme T_{hp}, T_{iair} operating temperatures pairs of 35, 18ºC and 45, 22ºC. With respect to th_c; the melting time increases very little with this parameter while, as discussed previously, the solidification time decreases considerably. In each arrangement, the melting time is mainly influenced by T_{hp}, whilst the solidification time depends strongly on T_{iair} and th_c. As to the variations in thickness and heating conditions: for PCM_A, melting and solidification last between 1.1 and 2.0 h and between 18.8 and 42.8 h, respectively, while for PCM_B these times range from 2.7 to 8.4 h and from 10.3 to 36.1 h. Comparing both arrangements, melting is much faster for PCM_A and solidification is faster for PCM_B. Due to the non-linear performance of PCM radiant floors, these differences depend strongly on the operating conditions, with rates that range from 2.6 to 4.2 for melting, and from 1.2 to 1.8 for solidification. Note that the melting process is too slow for PCM_B when T_{hp} equals 35ºC, with durations that range between 6.0 and 8.4 h depending on T_{iair} and th_c. This is mainly due to the distance from the heating pipes and the PCM subdomains make it difficult to thermo-activate the melting process at this temperature.

The time-averaged heat flux shown in Fig.10 increases with T_{hp} and decreases with T_{iair} for charging and discharging with extreme T_{hp}, T_{iair} operating temperatures pairs of 35, 22ºC and 45, 18ºC. The discharge time-averaged heat flux hardly varies with T_{hp}, as this temperature is the boundary conditions at the surface of the heating pipes during charging and only influence the initial heat flux when the discharge process commences. During this process, the boundary condition at the surface of the heating pipes is zero heat flux, being the same for all cases. The influence of th_c is considerable in the charge and discharge time-averaged heat fluxes, with higher values for the lower thickness of 10 mm. As to the variations in cover thickness and heating; for PCM_A charge and discharge time-averaged heat fluxes range from 31.5 to 82.5 W/m^2 and from 22.6 to 51.1 W/m^2, respectively; while for PCM_B, these heat fluxes range from 24.6 to 72.7 W/m^2 for charges and from 24.7 to 58.3 W/m^2 for discharges. Depending on the thermal conditions and the cover thickness, heat transfer rates are between 12 and 22% higher during charging and between 10 and 14% lower during discharging for PCM_A than for PCM_B.

4. CONCLUSIONS

Heat transfer during charge and discharge periods for classical and hydronic PCM radiant floors have been studied. In order to investigate the thermal performance, CFD models were developed for classical radiant floors made of concrete and conductive mortar, and for PCM floors with the PCM distributed in bands embedded in a concrete core.

For the steady-state, the heat transfer rates obtained for the CFD models were successfully compared with those calculated following the ASHRAE procedure.

Embedding of the PCM in the concrete core leads to a decrease in heat transfer, which depends on the temperature at the surface of the heating pipes, ranging from 50-110 W/m^2 for classical concrete radiant floors to 45-90 W/m^2 for PCM radiant floors.

The thermal energy stored increases, depending on the cover thickness, ranging between 445.5-552.0 Wh/m^2 for classical floors and 1141.0-1245.5 Wh/m^2 for PCM floors.

During discharge, PCM radiant floors release the thermal energy stored with stable heat fluxes near the time-averaged value during most of the discharge period.

Direct contact between the PCM and heating pipes, PCM_A, is essential to increase melting rates. Melting is up to 4.6 times faster for PCM_A than for PCM_B. In contrast, solidification is up to 1.8 times faster for PCM_B than for PCM_A.

The melting rates depend strongly on the temperature of the heating pipes during the charge, whilst solidification rates depend mainly on the indoor air temperature of the heated room and the cover thickness.

Heat transfer rates to the heated room are 12-22% higher for PCM_A than for PCM_B during charging and are 10-14% higher for PCM_B than PCM_A during discharging.

The PCM radiant floors tested by varying the temperature of the heating pipes and of the room provide wide ranges for the durations of the phase change processes and for the heat transfer rates. This thermal performance is suitable for radiant heating floors in households with different thermal qualities of the envelope.

ACKNOWLEDGMENTS

We wish to express our gratitude to the University Institute of Industrial Technology of Asturias (IUTA), the Ph.D. programme in Energy and Processes Control, University of Oviedo, and Gijon City Council for financial support under project SV-17-GIJÓN-1-22, which made this research work possible.

REFERENCES

[1] B.W. Olesen, Radiant floor heating in theory and practice, ASHRAE journal, 44 (2002) 19.

[2] B.W. Olesen, Control of floor heating and cooling systems, 7th REHVA World Congress-Climate (Clima 2000/Napoli 2001), 2001, pp. 15-18.

[3] M.S. Shin, K.N. Rhee, S.R. Ryu, M.S. Yeo, K.W. Kim, Design of radiant floor heating panel in view of floor surface temperatures, Building and Environment, 92 (2015) 559-577.
[4] ASHRAE, ASHRAE Handbook–HVAC Systems and Equipment, ASHRAE, Atlanta, 2016.
[5] ISO, ISO-11855 Building Environment Design-Design, Dimensioning, Installation and Control of Embedded Radiant Heating and Cooling Systems, International Organization of Standardization, Gèneve, Switzerland, 2012.
[6] K.-N. Rhee, B.W. Olesen, K.W. Kim, Ten questions about radiant heating and cooling systems, Building and Environment, 112 (2017) 367-381.
[7] Y. Konuklu, N. Şahan, H. Paksoy, 2.14 Latent Heat Storage Systems A2 - Dincer, Ibrahim, Comprehensive Energy Systems, Elsevier, Oxford, 2018, pp. 396-434.
[8] L. Navarro, A. de Gracia, S. Colclough, M. Browne, S.J. McCormack, P. Griffiths, L.F. Cabeza, Thermal energy storage in building integrated thermal systems: A review. Part 1. active storage systems, Renewable Energy, 88 (2016) 526-547.
[9] L. Navarro, A. de Gracia, D. Niall, A. Castell, M. Browne, S.J. McCormack, P. Griffiths, L.F. Cabeza, Thermal energy storage in building integrated thermal systems: A review. Part 2. Integration as passive system, Renewable Energy, 85 (2016) 1334-1356.
[10] B. Zalba, J.M. Marín, L.F. Cabeza, H. Mehling, Review on thermal energy storage with phase change: materials, heat transfer analysis and applications, Applied Thermal Engineering, 23 (2003) 251-283.
[11] R.K. Sharma, P. Ganesan, V.V. Tyagi, H.S.C. Metselaar, S.C. Sandaran, Developments in organic solid–liquid phase change materials and their applications in thermal energy storage, Energy Conversion and Management, 95 (2015) 193-228.
[12] N. Soares, J.J. Costa, A.R. Gaspar, P. Santos, Review of passive PCM latent heat thermal energy storage systems towards buildings' energy efficiency, Energy and Buildings, 59 (2013) 82-103.
[13] M. Pomianowski, P. Heiselberg, Y. Zhang, Review of thermal energy storage technologies based on PCM application in buildings, Energy and Buildings, 67 (2013) 56-69.
[14] K. Lin, Y. Zhang, X. Xu, H. Di, R. Yang, P. Qin, Experimental study of under-floor electric heating system with shape-stabilized PCM plates, Energy and Buildings, 37 (2005) 215-220.
[15] K. Lin, Y. Zhang, X. Xu, H. Di, R. Yang, P. Qin, Modeling and simulation of under-floor electric heating system with shape-stabilized PCM plates, Building and Environment, 39 (2004) 1427-1434.
[16] R. Barzin, J.J.J. Chen, B.R. Young, M.M. Farid, Application of PCM underfloor heating in combination with PCM wallboards for space heating using price based control system, Applied Energy, 148 (2015) 39-48.

[17] W. Cheng, B. Xie, R. Zhang, Z. Xu, Y. Xia, Effect of thermal conductivities of shape stabilized PCM on under-floor heating system, Applied Energy, 144 (2015) 10-18.

[18] X. Jin, X. Zhang, Thermal analysis of a double layer phase change material floor, Applied Thermal Engineering, 31 (2011) 1576-1581.

[19] Y. Xia, X.-S. Zhang, Experimental research on a double-layer radiant floor system with phase change material under heating mode, Applied Thermal Engineering, 96 (2016) 600-606.

[20] L. Cabrol, P. Rowley, Towards low carbon homes – A simulation analysis of building-integrated air-source heat pump systems, Energy and Buildings, 48 (2012) 127-136.

[21] J. Mazo, M. Delgado, J.M. Marin, B. Zalba, Modeling a radiant floor system with Phase Change Material (PCM) integrated into a building simulation tool: Analysis of a case study of a floor heating system coupled to a heat pump, Energy and Buildings, 47 (2012) 458-466.

[22] S. Lu, Y. Zhao, K. Fang, Y. Li, P. Sun, Establishment and experimental verification of TRNSYS model for PCM floor coupled with solar water heating system, Energy and Buildings, 140 (2017) 245-260.

[23] K. Huang, G. Feng, J. Zhang, Experimental and numerical study on phase change material floor in solar water heating system with a new design, Solar Energy, 105 (2014) 126-138.

[24] G. Zhou, J. He, Thermal performance of a radiant floor heating system with different heat storage materials and heating pipes, Applied Energy, 138 (2015) 648-660.

[25] M. Zhao, T. Zhu, C. Wang, H. Chen, Y. Zhang, Numerical simulation on the thermal performance of hydraulic floor heating system with phase change materials, Applied Thermal Engineering, 93 (2016) 900-907.

[26] V.R. Voller, C. Prakash, A fixed grid numerical modelling methodology for convection-diffusion mushy region phase-change problems, International Journal of Heat and Mass Transfer, 30 (1987) 1709-1719.

[27] V. Voller, C. Swaminathan, Genereral source-based method for solidification phase change, Numerical Heat Transfer, Part B Fundamentals, 19 (1991) 175-189.

[28] J. Jeon, S.-G. Jeong, J.-H. Lee, J. Seo, S. Kim, High thermal performance composite PCMs loading xGnP for application to building using radiant floor heating system, Solar Energy Materials and Solar Cells, 101 (2012) 51-56.

[29] F. Rouault, D. Bruneau, P. Sebastian, S.E. Ango, Numerical modeling and experimental study of a box-section tube bundle thermal energy storage for free-cooling of buildings, 12th Conference On Energy Storage, 2012.

[30] **rubitherm technologies GmbH,** Berlin, Germany https://www.rubitherm.eu/ https://www.rubitherm.eu/media/products/datasheets/Techdata_-RT28HC_EN_06082018.PDF acc(eses 10 of june 2020)

[31] H. Jamil, M. Alam, Sanjayan J.,, J. Wilso, Investigation of PCM as retrofitting option to enhance occupant thermal comfort in a modern residential buildingn, Energy and Buildings 133 (2016) 217–229. http://dx.doi.org/10.1016/j.enbuild.2016.09.064

[32] C.T. de la Edificación, Documento básico HE Ahorro de energía, CTE, DB-HE, (2013).

[33] A.H. Mosaffa, F. Talati, M.A. Rosen, H.B. Tabrizi, Approximate analytical model for PCM solidification in a rectangular finned container with convective cooling boundaries, International Communications in Heat and Mass Transfer, 39 (2012) 318-324.

[34] A. Felix Regin, S.C. Solanki, J.S. Saini, An analysis of a packed bed latent heat thermal energy storage system using PCM capsules: Numerical investigation, Renewable Energy, 34 (2009) 1765-1773.

[35] P. Dolado, A. Lazaro, J.M. Marin, B. Zalba, Characterization of melting and solidification in a real scale PCM-air heat exchanger: Numerical model and experimental validation, Energy Conversion and Management, 52 (2011) 1890-1907.

[36] M. Rostamizadeh, M. Khanlarkhani, S. Mojtaba Sadrameli, Simulation of energy storage system with phase change material (PCM), Energy and Buildings, 49 (2012) 419-422.

[37] M.M. Prieto, B. González, Fluid flow and heat transfer in PCM panels arranged vertically and horizontally for application in heating systems, Renewable Energy, 97 (2016) 331-343.

[38] M.M. Prieto, I. Suárez, B. González, Analysis of the thermal performance of flat plate PCM heat exchangers for heating systems, Applied Thermal Engineering, 116 (2017) 11-23.

[39] A.V. Arasu, A.S. Mujumdar, Numerical study on melting of paraffin wax with Al2O3 in a square enclosure, International Communications in Heat and Mass Transfer, 39 (2012) 8-16.

[40] L. Solomon, A.F. Elmozughi, A. Oztekin, S. Neti, Effect of internal void placement on the heat transfer performance – Encapsulated phase change material for energy storage, Renewable Energy, 78 (2015) 438-447.

[41] A.A. Al-abidi, S. Bin Mat, K. Sopian, M.Y. Sulaiman, A.T. Mohammed, CFD applications for latent heat thermal energy storage: a review, Renewable and Sustainable Energy Reviews, 20 (2013) 353-363.

[42] A. Inc, ANSYS Meshing User's Guide.

[43] N.S. Dhaidan, J.M. Khodadadi, Melting and convection of phase change materials in different shape containers: A review, Renewable and Sustainable Energy Reviews, 43 (2015) 449-477.

[44] W. Youssef, Y.T. Ge, S.A. Tassou, CFD modelling development and experimental validation of a phase change material (PCM) heat exchanger with spiral-wired tubes, Energy Conversion and Management, 157 (2018) 498-510.

[45] A. Inc., ANSYS FLUENT Theory Guide.

[46] TSI, Turkish Standard 11261-Fundamentals of design for floor heating systems, Turkish Standards Institute, Ankara, 1994.

TABLES

Table 1. Thermal properties

Materials (cell zones)	ΔT_{melt} (ºC)	ρ (kg/m^3)	c_p (J/kg·K)	k (W/m·K)	μ (kg/m·s)	λ (kJ/kg)
RT28HC (PCM)	27-29	770-880	2000	0.2	0.00239	224
Concrete	-	1800	1050	0.93	-	-
Conductive mortar	-	1600	950	2	-	-
XPS (Insulation)	-	30	1260	0.028	-	-
Wood (Cover)	-	70	2310	0.173	-	-

Table 2. PCM floors grid test. Δt=0.5s, A_{mush}=10^5, th_c= 20 mm, T_{iair}= 20ºC, T_{hp}= 40ºC

Grid Refinement	Floor case	Elements	Mesh quality Avg.	Mesh quality St. dev.
1	PCM_A	3647	0.91	0.075
	PCM_B	3775	0.90	0.071
2	PCM_A	8196	0.92	0.067
	PCM_B	8490	0.92	0.062
3	PCM_A	14836	0.92	0.063
	PCM_B	15356	0.92	0.058

Table 3. Main parameters of the floors for the application of the method proposed by ASHRAE

Floor case	th_c (mm)	th_{uhp} (mm)	k_{uhp} (W/mK)	R_c (m^{2}ºK/W)	R_{uhp} (m^{2}K/W)	R_{tot} (m^{2}K/W)	f (m^{-1})	η (-)
CONC	10	10	0.93	0.058	0.011	0.169	20.813	0.487
	20	10	0.93	0.116	0.011	0.227	19.569	0.535
MORT	10	40	2	0.058	0.020	0.178	7.504	0.859
	20	40	2	0.116	0.020	0.236	7.578	0.869
PCM_A,B	10	10	0.565	0.058	0.018	0.176	25.086	0.413
	20	10	0.565	0.116	0.018	0.234	22.992	0.468

Table 4. Maximum floor surface temperature (MFST) and difference between the maximum and minimum floor surface temperature (DFST) at the floor surface for th_c= 20 mm, T_{iair}= 20ºC, T_{hp}= 40ºC and several times.

CONC							
	Charge			Discharge			
t(h)	0.5	2	6	8	11	16	21
MSFT	24.5	27.3	28.0	25.2	23.5	21.8	20.9
DFST	4.5	4.9	2.5	0.05	0.08	0.04	0.02
MORT							
	Charge			Discharge			
t(h)	0.5	2	6	8	11	16	21
MSFT	22.4	26.8	27.9	25.9	23.6	21.6	20.7
DFST	1.9	1.7	0.9	0.2	0.1	0.05	0.02
PCM_A							
	Charge			Discharge			
t(h)	0.5	2	6	8	11	16	21
MSFT	24.5	27.4	28.0	24.9	24.0	23.9	23.7
DFST	4.5	3.6	3.7	0.8	0.8	1.4	1.4
PCM_B							
	Charge			Discharge			
t(h)	0.5	2	6	8	11	16	21
MSFT	24.5	26.3	28.0	24.5	24.0	23.7	23.5
DFST	4.5	4.3	4.1	0.5	0.3	0.3	0.3

Table 5. Thermal energies supplied, released and stored during charging and complete discharging for T_{iair}= 20ºC, T_{hp}= 40ºC.

Radiant Floor	th_c (mm)	E_{hp} (Wh/m^2)	$E_{fs,char}$ (Wh/m^2)	$E_{bs,char}$ (Wh/m^2)	$E_{fs,dis}$ (Wh/m^2)	$E_{bs,dis}$ (Wh/m^2)	TES (Wh/m^2)	TES (%)
CONC	10	908.5	395.0	27.5	446.0	40.5	486.0	53.5
	20	866.0	286.0	28.0	495.0	57.0	552.0	63.7
MORT	10	952.0	469.0	37.5	412.0	34.0	445.5	46.8
	20	893.5	340.5	38.0	465.0	49.5	515.0	57.6
PCM_A	10	1584.0	375.5	26.0	1092.0	90.5	1182.5	74.7
	20	1546.0	274.0	26.5	1121.0	124.5	1245.5	80.6
PCM_B	10	1482.0	320.0	21.0	1055.0	86.0	1141.0	77.0
	20	1440.0	227.0	21.0	1074.0	118.0	1192.0	82.8

FIGURES

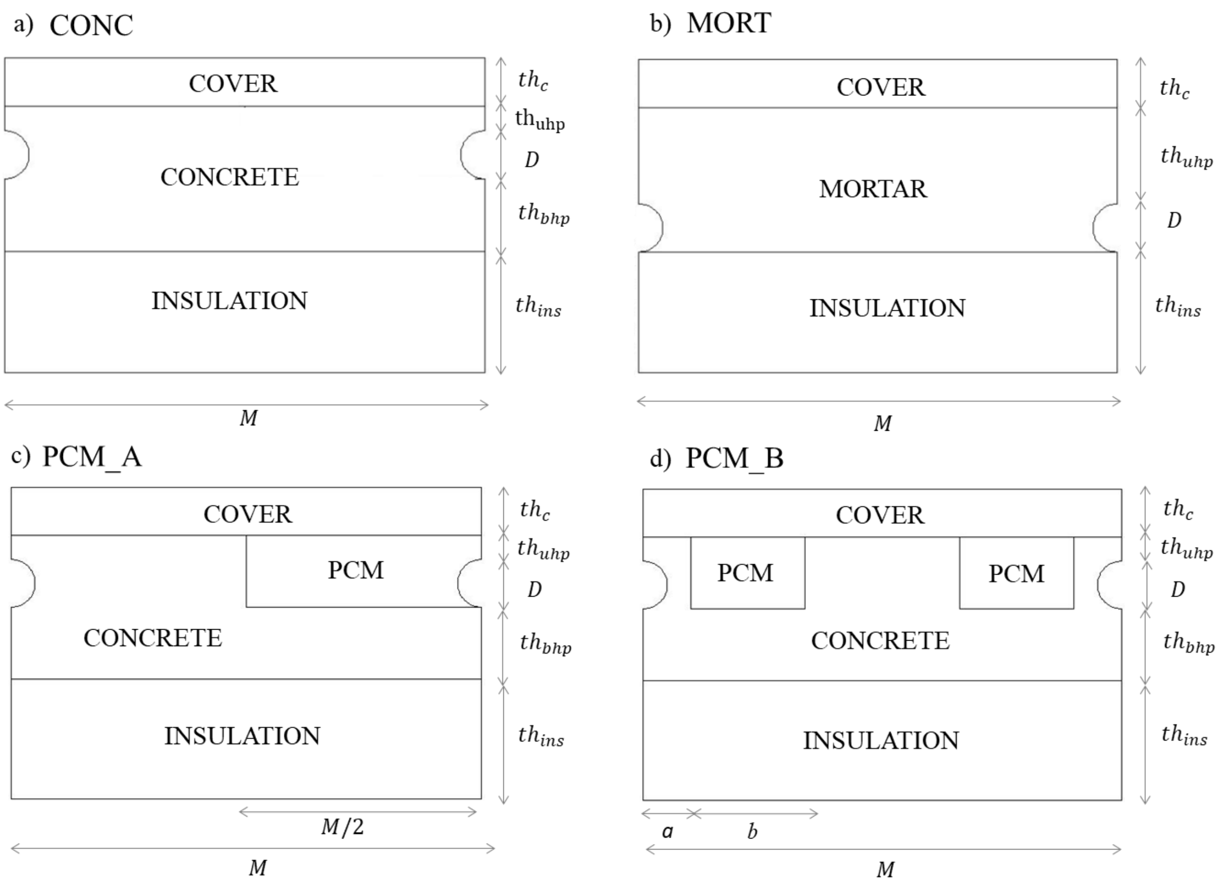

Figure 1. Computational domain: convectional (a, b) and PCM (c, d) radiant floors.

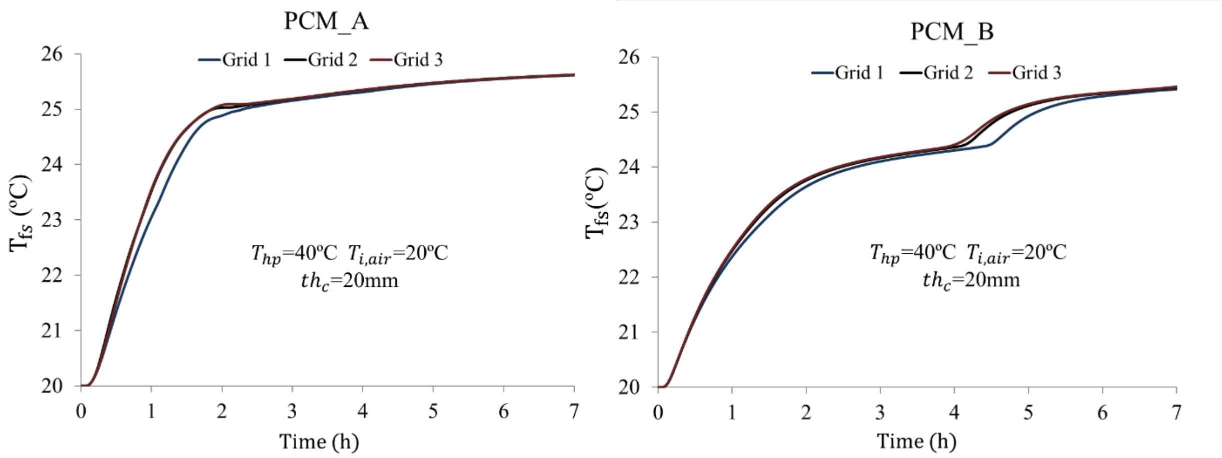

Figure 2. Grid test results for PCM floors for Δt=0.5s, A_{mush}=10^5, th_c= 20 mm, T_{iair}= 20ºC, T_{hp}= 40ºC.

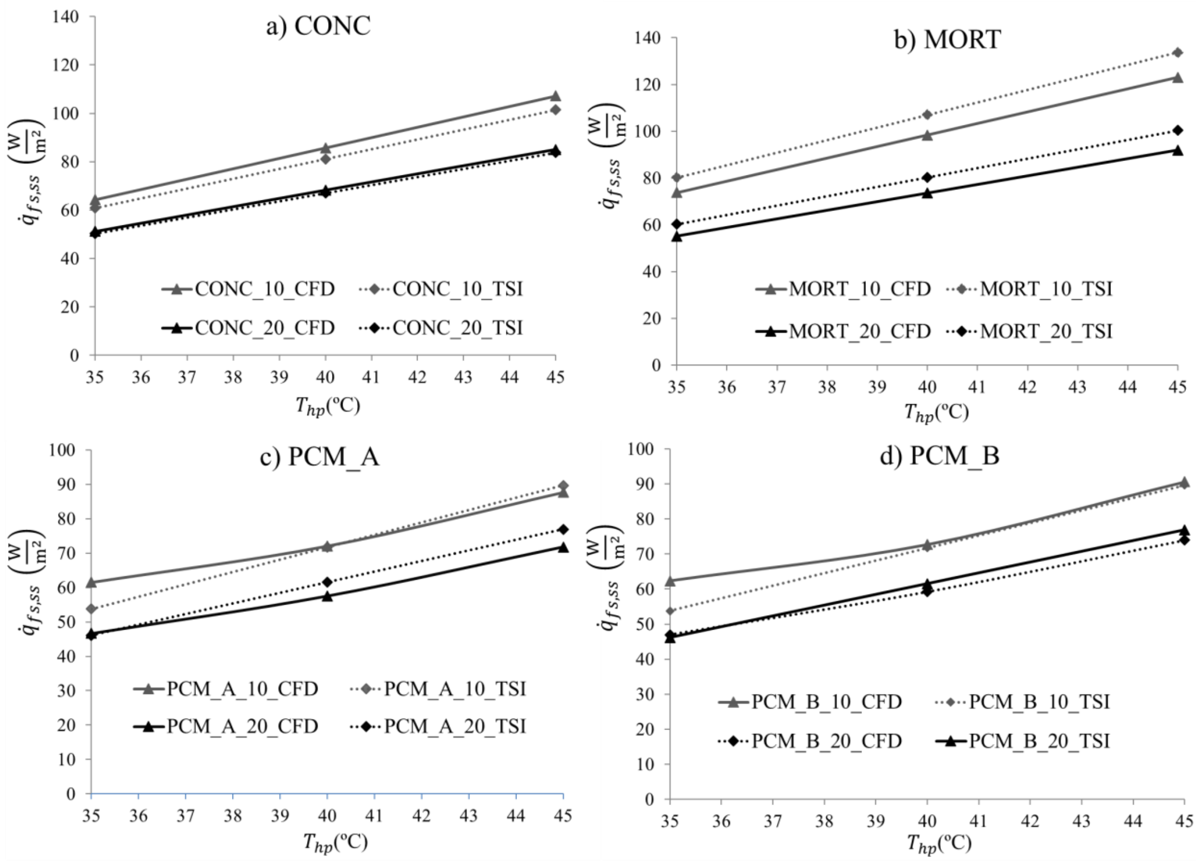

Figure 3. Steady-state heat transfer rates computed by CFD and TSI (proposed by ASRHAE) procedures for T_{iair}=20ºC.

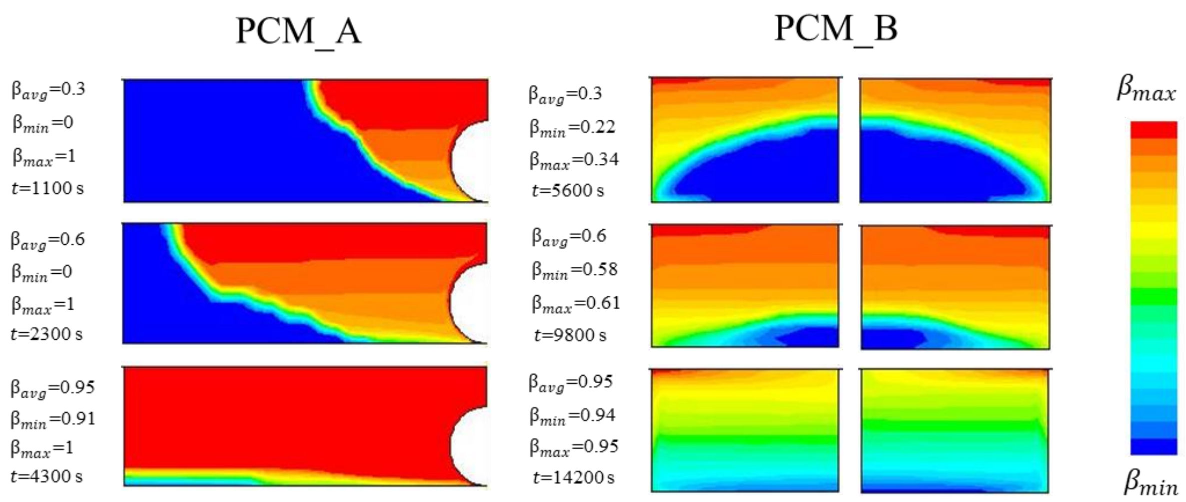

Figure 4. Melted liquid fraction in PCM subdomains for th_c= 20 mm, T_{iair}= 20ºC, T_{hp}= 40ºC.

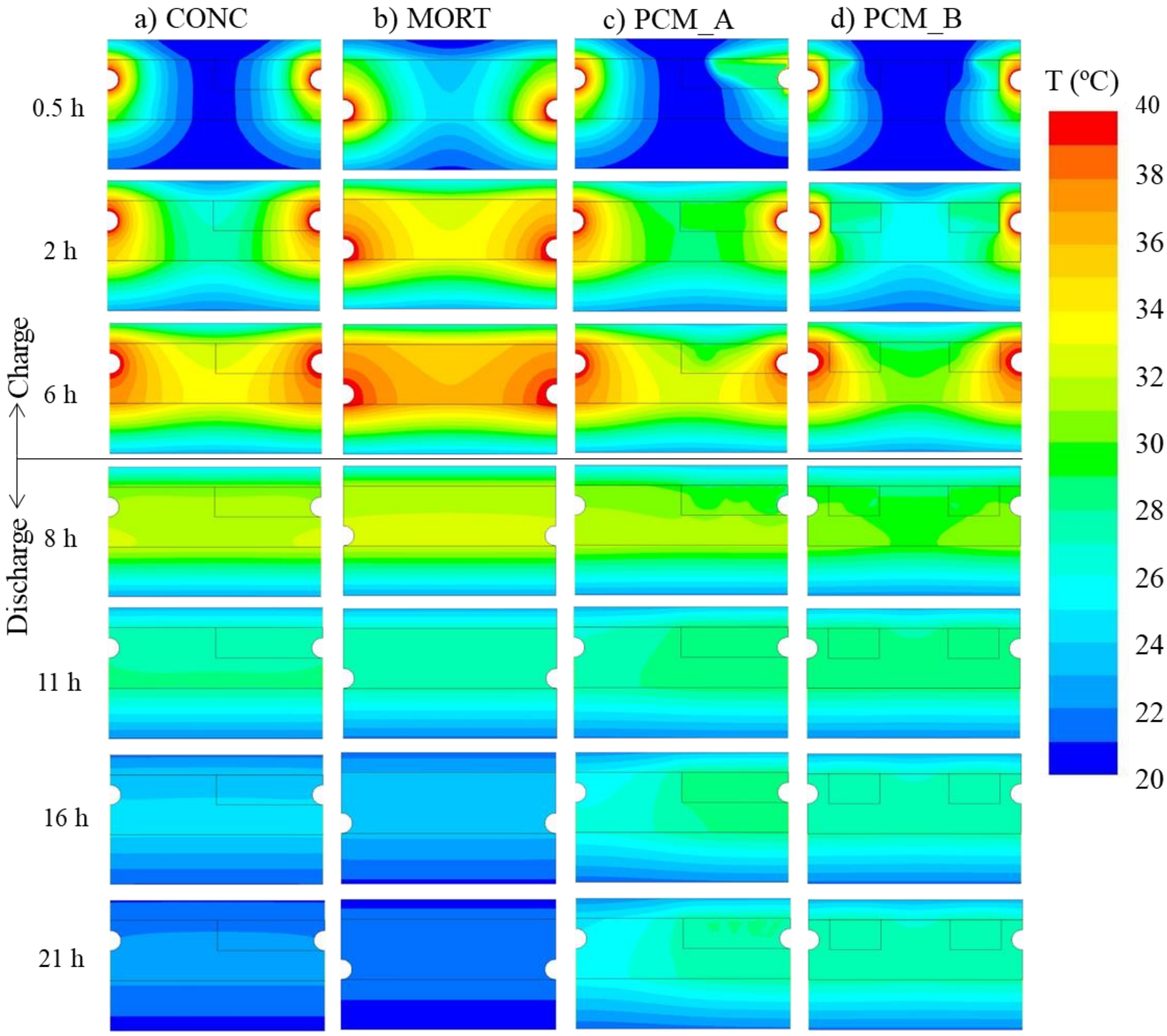

Figure 5. Temperature contours in the materials of the radiant floors for the charge and the discharge for th_c= 20 mm, T_{iair}= 20ºC, T_{hp}= 40ºC.

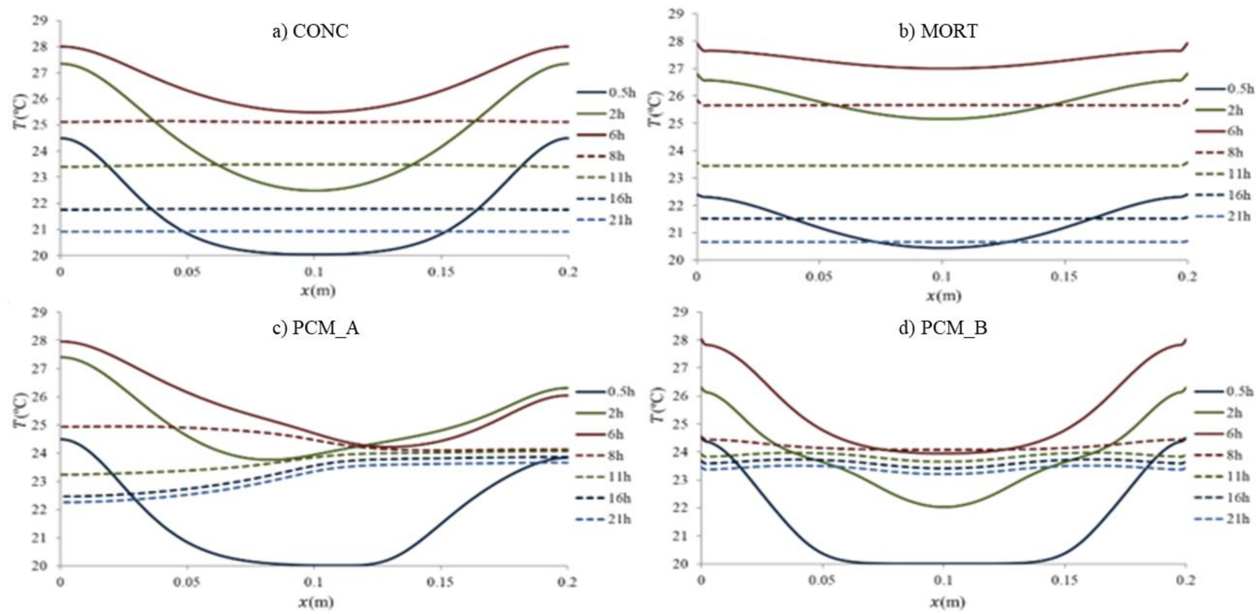

Figure 6. Temperature distribution during the discharge at points on the surface of the radiant floors for th_c= 20 mm, T_{iair}= 20ºC, T_{hp}= 40ºC.

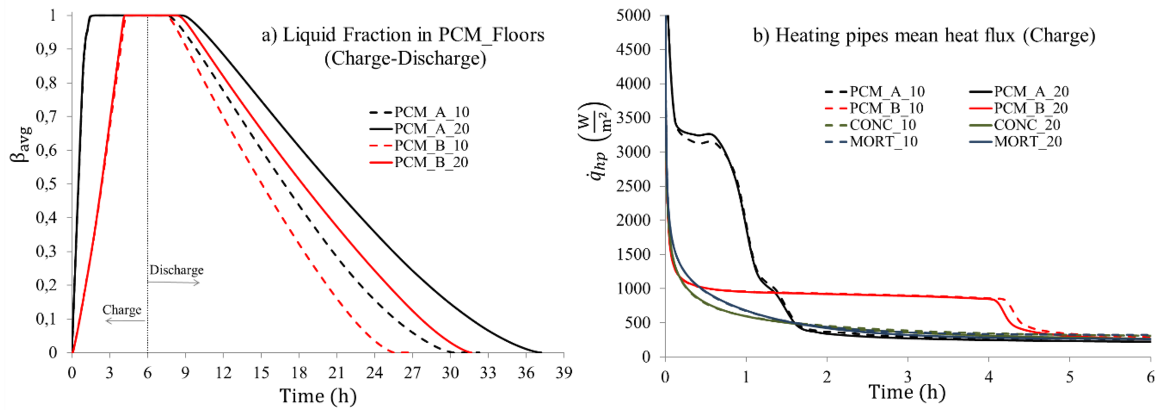

Figure 7. Evolution of averaged variables for T_{iair}= 20ºC and T_{hp}= 40ºC as a function of the cover thickness: a) liquid fraction for PCM floors during charging and discharging, and b) heat fluxes for the four radiant floors at the surface of the heating pipes during charging.

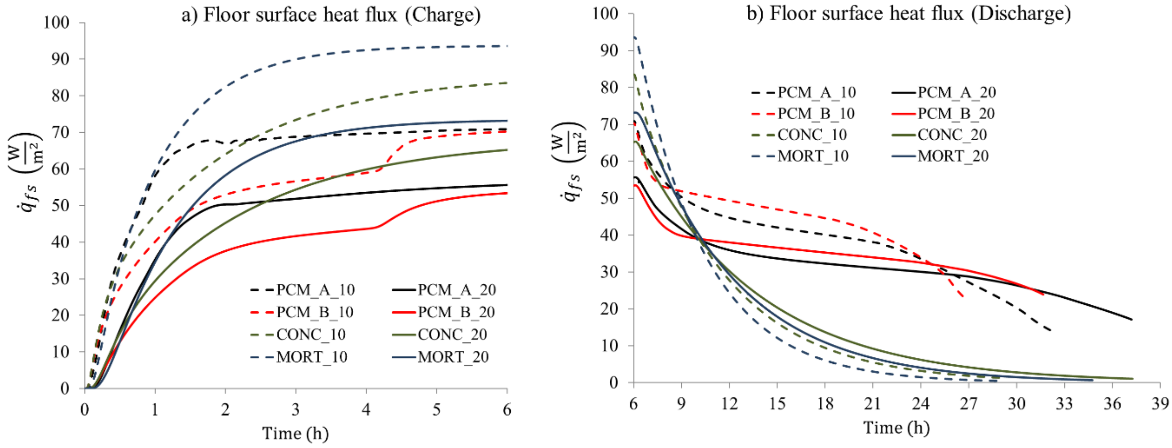

Figure 8. Evolution of the averaged heat fluxes at the surfaces of the radiant floors for T_{iair}= 20ºC and T_{hp}= 40ºC as a function of the cover thickness: a) charging b) discharging.

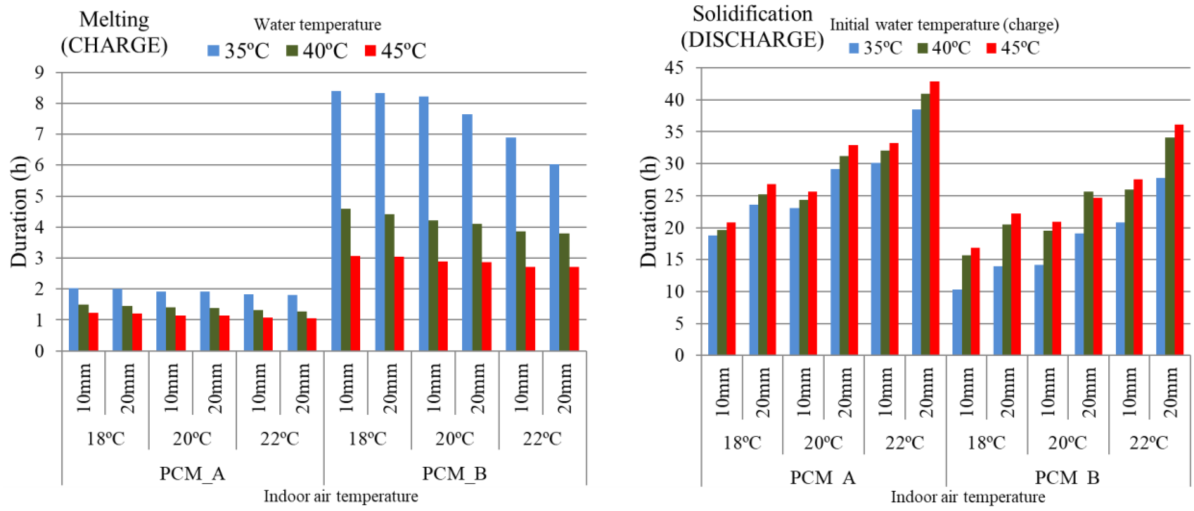

Figure 9. Melting and solidification times for PCM floors according the temperature of the water inside the pipes, room temperatures and cover thickness.

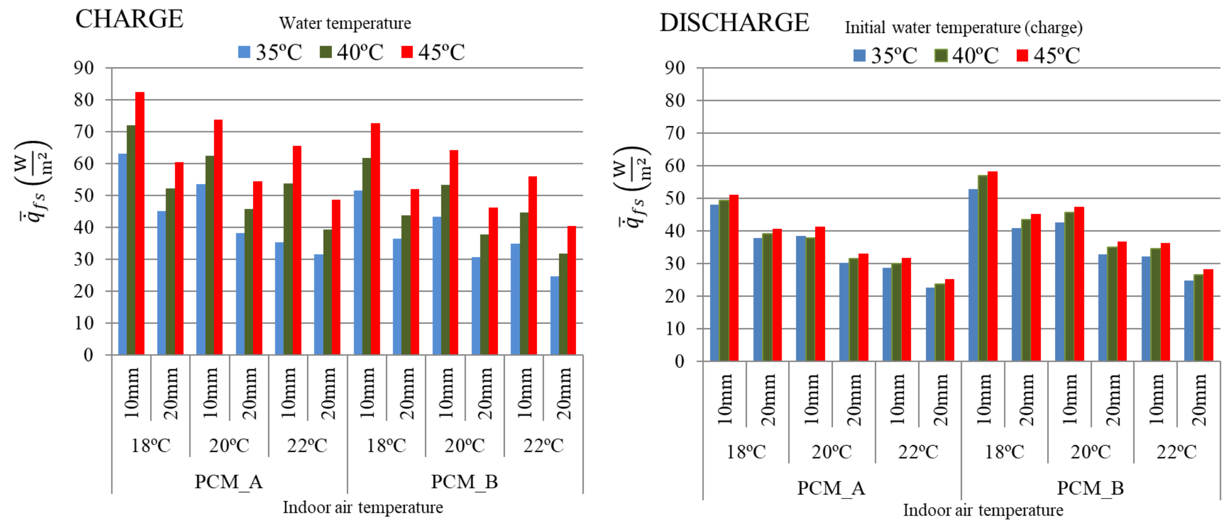

Figure 10. Time-averaged heat fluxes at floor surface during charging and discharging for PCM floors depending on conditions: the temperature of the water inside the pipes, room temperatures and cover thickness.